Estimating Object Hardness with a GelSight Touch Sensor

Wenzhen Yuan[1], Mandayam A. Srinivasan[2] and Edward H. Adelson[3]

***Abstract*— Hardness sensing is a valuable capability for a robot touch sensor. We describe a novel method of hardness sensing that does not require accurate control of contact conditions. A GelSight sensor is a tactile sensor that provides high resolution tactile images, which enables a robot to infer object properties such as geometry and fine texture, as well as contact force and slip conditions. The sensor is pressed on silicone samples by a human or a robot and we measure the sample hardness only with data from the sensor, without a separate force sensor and without precise knowledge of the contact trajectory. We describe the features that show object hardness. For hemispherical objects, we develop a model to measure the sample hardness, and the estimation error is about 4% in the range of 8 Shore 00 to 45 Shore A. With this technology, a robot is able to more easily infer the hardness of the touched objects, thereby improving its object recognition as well as manipulation strategy.**

I. Introduction

For both humans and robots, the sense of touch is important for object recognition and dexterous manipulation [1]. When we touch an object, we quickly learn a set of its physical properties, such as the shape, smoothness, hardness, thermal conductivity, etc. Those properties enable us to quickly categorize the object and devise a suitable manipulation strategy. Considerable research has been conducted to infer tactile object properties using robots as well. Two recent examples are Drimus et al. [2] and Chu et al. [3], who introduced methods to infer multiple object properties by analyzing touch sensor input during several controlled exploration procedures.

Among the physical properties of objects, hardness is particularly important. Many objects have distinct hardness and which makes them easier to recognize, such as human or animal bodies, cushions, sponges, food, and fabrics. A robot would benefit from hardness detection to recognize those objects in daily tasks and choose proper contact force to avoid damage. Hardness is also helpful in specific jobs, like product evaluation. For many fruits, like avocado, peach, tomato, hardness indicates the level of ripeness. It would be helpful to have a robot that is capable of estimating whether a fruit is ready to eat by measuring its hardness. Palpation of human tissue has diagnostic value and is useful in guiding tele-surgery.

[1]Department of Mechanical Engineering, and Computer Science and Artificial Intelligence Laboratory(CSAIL), MIT, Cambridge, MA 02139, USA yuan_wz@csail.mit.edu

[2]Laboratory for Human and Machine Haptics (MIT TouchLab), Research Laboratory of Electronics and Department of Mechanical Engineering, MIT, Cambridge, MA 02139, USA and UCL TouchLab, Computer Science Department, UCL, London, UK srini@mit.edu

[3]Department of Brain and Cognitive Sciences and CSAIL, MIT, Cambridge, MA 02139, USA adelson@csail.mit.edu

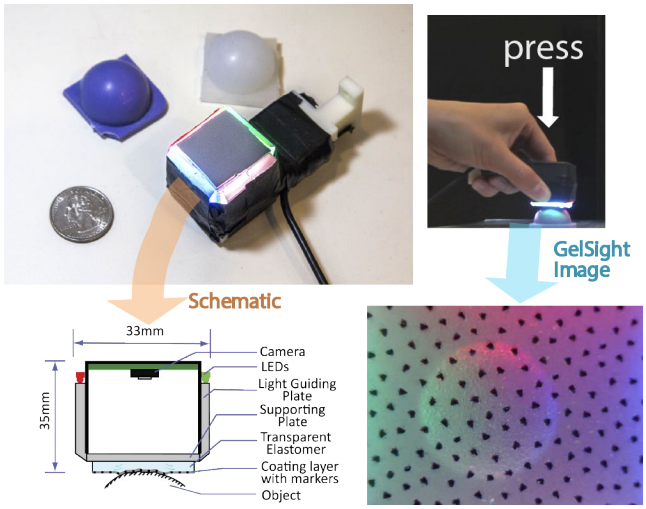

Fig. 1. The fingertip GelSight sensor and hemispherical silicone samples used in this project. We manually press the sensor on samples, and infer sample hardness from GelSight data sequences.

Hardness can be described in terms of deformation as a function of force, suggesting the need for accurate force sensing in the process. However, humans are surprisingly good at estimating hardness with a passive fingertip, via cutaneous touch alone, evidently based on the deformation pattern of the fingertip [4]. We wish to replicate this capability in a robot fingertip, allowing more convenient hardness estimation when the contact force is unknown or poorly controlled.

Object hardness is generally measured by touch, but there are several challenges. It can be measured, for example, by comparing the contact pressure and indentation depth between the touch sensor and the contact object. However, different object geometries give rise to different contact forces, correlation the two is complicated, and measuring the object shape to sufficient precision is difficult for most touch sensors. There are several but limited attempts to measure object hardness by tactile sensors, but they work only under strict conditions, like the precise control of contact movement and the single geometry or type of the objects.

We have attempted to expand the robot's ability to estimate object hardness with an optical based touch sensor GelSight [5], [6]. The sensor takes high-resolution tactile images of the contact geometry and deformation distribution. We press the sensor against a set of silicone samples, as shown in Figure 1, and get a set of data during the press, and show some example results in Figure 2. The movement is intentionally imprecise; it is performed by a human holding the sensor,

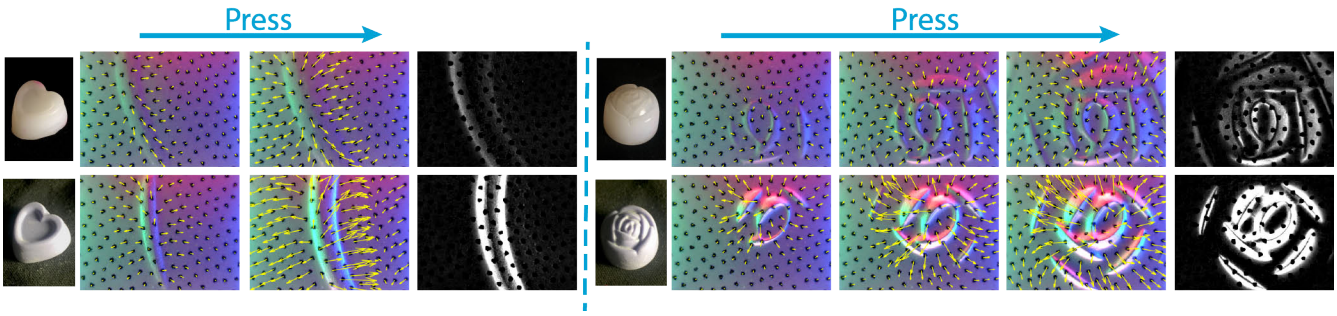

Fig. 2. GelSight data when pressing on silicone samples of different hardness. Samples in the first row have a hardness of 35 in Shore 00 scale, the samples on the second row are 72 in Shore 00 scale. In each set of images, the colored figures are the images captured by GelSight camera, with the movement of markers shown in arrow field; they are taken in different pressing stages. The gray images show the gradient on contact surface under the largest force.

without exact control of the trajectory or force. We find that the two major features that are monotonically related to sample hardness are the brightness change in the GelSight image, and the magnitude of marker field expansion. The brightness change in GelSight images infer the surface normal of the contact region, and the marker field expansion is related to the pressing force. For the hemispherical objects, we proposed a model to quantify the features to predict the sample hardness. Experiments show that the model works for hemispheres of different radii, with a mean estimation error of less than 5 in the Shore 00 scale.

This paper makes the following contributions:

1) Proposes a method of using a touch sensor to estimate object hardness through loosely controlled contact, which could be initiated by a human or a loosely controlled open-loop robot arm. The method is much less constrained regarding contact conditions and object shapes than previous attempts, which makes it promising for daily robotic tasks for recognition and manipulation.
2) Proposes a model to measure hardness of 12 hemisphere silicone samples within the hardness range of 8 in Shore00 scale to 45 in Shore A scale. The measurement precision and resolution is much higher than what has been reported in the literature.

II. Related Work

A. Hardness Measurement

Human observers will often press or poke and object to judge its hardness [7], [8]. Srinivasan and LaMotte [4] showed with experiments that humans can estimate hardness very well with a passive fingertip, via cutaneous touch alone, evidently based on the deformation pattern of the fingertip and that kinesthetic information is not essential. However, there is limited research on making a robot achieve a similar capability, and existed methods have strict constrains, mostly on loading controls, object geometry or categories.

For a robot, the most straightforward way to measure object hardness is by applying controlled force and measuring deformation, or vice versa [9]. Using BioTac, a commercially available tactile sensor which measures the overall pressing pressure, vibration, coarse pressure distribution and heat conductivity, Su et al. [10] measured the hardness of flat rubber samples. They mounted the BioTac sensor on a robot hand fingertip, and strictly controlled the fingertip motion to press on the flat silicone samples with fixed speed, and recorded the force measured by one of the electrodes on the sensor. They showed the force signal gives rise to different curves for the 6 samples on the range of 30 Shore00 rubber to aluminum make some difference. However, for this method to be applicable, the sensor movement and object geometry should be strictly controlled, and the authors did not propose a direct model to measure object hardness.

A less restricted way to measure hardness is to design a touch sensor of some special structures that can automatically measure the local force and pressing depth. An example is that demonstrated by Shimizu et al. [11]. They designed a sensing cell with a gas chamber and piezo-resistance to measure the indentation of the mesa on its top surface. The cell thus measures the material hardness from the force measured by pressure change in the chamber and the indentation depth measured by piezo-resistance. The sensor makes measurement easier, under the condition that the suface geometry is certain; the sensor itself can hardly be used for other touch tasks. Okamoto et al. [12] introduced a round shaped soft tactile sensor with strain gauges embeded that measures object roughness, friction, and hardness. They showed that the sensor has distinctive output signals when testing three samples with different Young's moduli. But the sensor still has strict requirement on the loading control and sample shapes.

There are also some sensors designed specifically for measuring hardness for medical use, such as [13], [14]. Another method is to correlate the ultrasonic signal and tissue hardness and researchers have designed structures to measure vibration and resonance frequency for tissue tests [15]. Unfortunately, those sensors are not generalized for measuring hardness of common objects or using in other tactile tasks.

B. Optical Touch Sensors

Optical touch sensors make a category of touch sensors that convey the force or shape information resulting from

touch into optical signals, and employ the optical signal to infer contact conditions and object properties. Most commonly, the optical touch sensors use a piece of deformable material as contact medium, and apply an optical method to measure the deformation of the contact medium. [16], [17], [18] have proposed optical based tactile sensors in which markers on the contact medium are tracked by cameras and a model is built to measure contact force from marker displacement. Optical touch sensors typically have a soft touch interface and high sensing resolution. However, due to the complex mechanistic properties of the rubber or fluid medium, it is usually challenging to measure the force distribution accurately when an optical touch sensor is contacting an arbitrary surface.

A GelSight touch sensor is also an optical touch sensor, but is designed to infer high-resolution shape of the contact interface as its basic measurement goal. It consists of a clear elastomeric slab covered with a reflective membrane, along with an embedded camera and a lighting system [5], [6]. On contact with an object, the resulting deformation height map of the membrane is derived via photometric stereo. The sensor can resolve features in the micron range. Jia, et al. [19] showed that it was better than human subjects in detecting lumps in a soft medium. Li [20] proposed a fingertip GelSight device, which is small enough to be mounted on a robot fingertip. Due to constraints on size and weight, this device has resolution of tens of microns, and does not provide a high precision height map. Yuan et al. [21] further improved the sensor by adding markers on the sensor surface and track their movement, and thus enhancing its ability to infer the approximate contact force on the sensor. With a GelSight sensor, a robot would not only be able to quickly determine the shape and texture of an object, but also infer more physical properties that remain to be explored.

In this paper, the proposed method begins with a qualitative observation: the tactile image sequences from GelSight look quite different for hard objects versus soft ones. When a hard object is pressed, it retains its shape as force increases. In contrast, a soft object's shape flattens out as force increasess, and the depression is distributed more uniformly over the contact area. In addition, the boundary of the contact region is more pronounced for a hard object than for a soft one. This suggests that it is possible for a GelSight sensor to estimate hardness even when the force is unknown or poorly controlled, as may occur in the real world situations.

III. Experimental Setup

We used a fingertip GelSight device that is introduced in [20], with black markers on the surface to track the displacement field. The elastomer on GelSight is $25\text{mm} \times 25\text{mm} \times 1.7\text{mm}$, and the average interval between the black markers is about 1.1mm. The hardness of the elastomer is 55 in Shore00 scale. The USB camera within the sensor takes images of size 960×720 pixels over an area of $18.4\text{mm} \times 13.8\text{mm}$.

In this set of experiments, we estimate object hardness by pressing the GelSight sensor on samples, and analyze the sensor's signal to determine the hardness. The samples are made of silicone rubber casted by different molds. The hardness is measured on the Shore 00 scale using a dial durometer (PTC 470). We denote rubber with a rating of 35 on the Shore 00 scale as Shore0035. We combined soft and hard silicone materials (Smooth-on, Inc.) in variable ratios to achieve 12 hardness degrees ranging from Shore0008 to Shore0083. (Note that Shore0083 maps to 45 on the Shore A scale). The hardness range is roughly that of a gummy bear to a pencil eraser. The hemispherical samples have 4 different radii: 30mm, 19mm, 12.7mm and 9.5mm.

IV. Experimental Procedure

In the hardness measurement experiment, a sample is placed on a hard flat surface, and the sensor is manually pressed on the sample by the human tester, in the approximately vertical direction, as shown in Figure 1. The tester is asked to press the sensor in a natural way, so the procedure is similar to human behavior for touching and feeling the hardness of an object. In the process, the sensor output can be used to estimate normal force and normal deformation. However, as the press is performed by a human, exact trajectory can not be predicted. As a result, the pressing velocity and force is unknown and uneven, and there are also unintended shear force or torque on the contact surface. Those interferences normally occur in the field tasks for robot exploration or manipulation, and cause difficulties for testing.

We also mounted the sensor on a Baxter robot and designed a loosely controlled open-loop movement for the robot to press the sensor on silicone samples. The data are used as test datasets for verification of the hardness prediction method derived from human tests.

To reduce the sensor's error due to illumination bias, we required the sensor to contact samples centrally. In practice, we performed multiple presses, and chose 3 or 4 presses that were within a acceptable range. During the press, as the normal force grows and then descends to 0, the indentation depth and contact area also increase and decrease. We consider only the loading period, in order to reduce the influence of silicone viscoelasticity.

V. Data Processing

We hypothesize that the relationship between the geometry of the deformed object and the pressing force are the most important clues to show the object hardness. When pressing on harder samples, the object deforms less, thus retaining larger slopes on the contact surface, and the normal force is relatively larger at lower depths of indentation. The contact geometry is reflected by a brightness change in the GelSight image, and the contact force is inferred from the marker displacement field. We thus consider these two kinds of signals as our major measures.

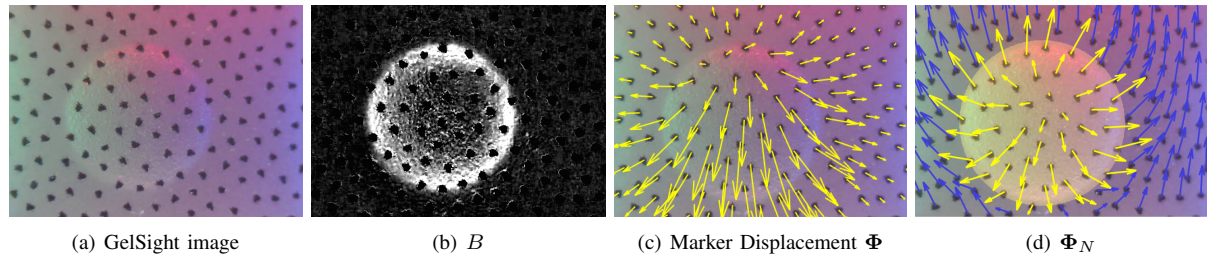

(a) GelSight image (b) B (c) Marker Displacement $\mathbf{\Phi}$ (d) $\mathbf{\Phi}_N$

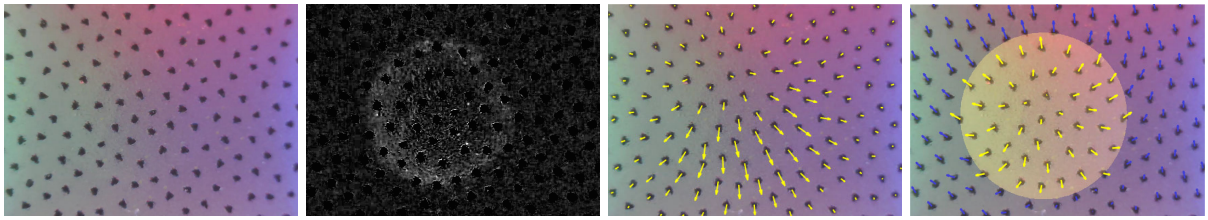

(e) GelSight image (f) B (g) Marker Displacement $\mathbf{\Phi}$ (h) $\mathbf{\Phi}_N$

Fig. 3. GelSight data when pressing on R12.7mm samples. The first row is the data of a Shore0072 sample, the second row is of a Shore0035 sample. These particular frames are taken from pressing sequences and specifically chosen to have similar contact area. (b) and (f) show the brightness change function B, and the bright circles in the center denote contact area. (c) and (g) show the displacement field of the markers $\mathbf{\Phi}$; (d) and (h) show the $\mathbf{\Phi}_N$ field decomposed from $\mathbf{\Phi}$, which is caused only by normal force. Contact area is shown by light yellow color in (d) and (h).

A. Shape Change during Press

The change of contact geometry is inferred from the brightness change of GelSight images. The brightness change is a function of surface normal of the contact surface [5], and the sensor integrates the surface gradient to obtain the heightmap. For the fingertip GelSight device, due to the simplification of the illumination system, the surface normal measurement is not precise, while the error accumulates when calculating the heightmap. To reduce the accumulation error, we use the surface gradient directly instead of heightmap. In practice, we use a function $B(r, g, b, r_0, g_0, b_0)$, which is a monotonical function to surface normal magnitude, to represent the change of surface geometry. In the function, r, g, and b are the value changes in the 3 color channels on a single pixel, and r_0, g_0, and b_0 are the original values.

Figure 3(b)(f) shows the brightness function B of GelSight when the sensor is pressed on different samples. (Note that the black marker areas are excluded when calculating B) The significant circular area or large B is the contact area with the hemispherical samples. We measure the contact area according to B, and denote the radius of the area as $R_{\max}$. For the same sample, $R_{\max}$ is monotonically related to the pressing force and depth. Within the contact area, B grows larger when approaching the border, indicating larger surface normal values. When pressing on the softer samples, B is much smaller, because the sample deforms more and is flatter at the top. We compare B in the two cases in Figure 4. As the geometry of the samples and the contact area is rotationally symmetric, pixels at the same radius R along the contact center are expected to have the same absolute slope. Therefore, we measure the mean value of B at radius R, and denote it as $\bar{B}(R)$. Figure 4 shows $\bar{B}(R)$ distribution for Figure 3(b) and Figure 3(f). The overall $\bar{B}(R)$ is significantly smaller for a softer sample. We fit the increasing part of

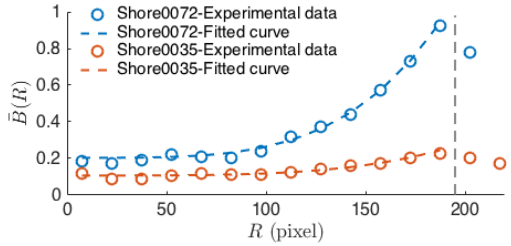

Fig. 4. Mean brightness function value $\bar{B}(R)$ along the radius R of contact area, corresponding to Figure 3(b) and (f). The fitted curve is fourth degree binomial $\hat{B}(R) = p_1 \times R^4 + p_0$. The gray dashed line denotes the contact border.

$\bar{B}(R)$ with a binomial function $\hat{B}(R) = p_1 \times R^4 + p_0$, and denote the peak value as $\bar{B}_{\max}$.

We use $\bar{B}_{\max}$ and p_1 to indicate the sample hardness. When pressing on the hemispherical samples with a radius of 12.7mm, the relationship of $\bar{B}_{\max}$ to the contact radius $R_{\max}$ is shown in Figure 5(a), which is close to a linear relationship $\bar{B}_{\max}(R_{\max}) = f_B \times R_{\max} + p_0$, and the linear coefficient f_B is monotonically related to the hardness. The relation of f_B to the hardness is shown in Figure 5(b). We fit the data with an offset exponential function $\hat{f}_B = A_B \exp(B_B \times H) + C_B$, so that if we measure f_B from a sequence of GelSight data during a press, we can predict the hardness $\hat{H}_B$ using $\hat{f}_B$.

The coefficient p_1 in the fitted curve $\hat{B}(R) = p_1 \times R^4 + p_0$ is also related to the contact radius $R_{\max}$, and the relation differs as the sample hardness differs. The relationship of p_1 to $R_{\max}$ in logarithmic scale is shown in Figure 6. The relationship between p_1, $R_{\max}$ and the predicted sample hardness $\hat{R}$ can be approximated as

$$\begin{bmatrix}\log(p_1) & \log(R_{\max}) & 1\end{bmatrix} \mathbf{b} = \hat{H}. \quad (1)$$

We use linear regression to obtain $\mathbf{b}$ from the training data set, and make a prediction of hardness $\hat{H}_p$ by averaging all

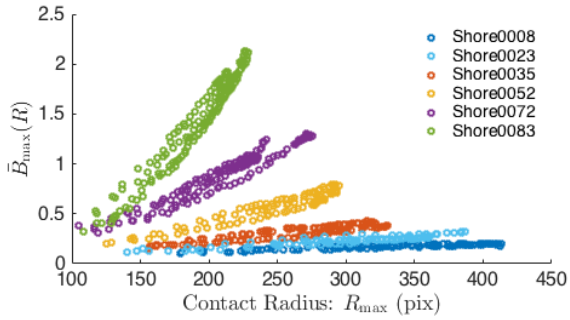

(a)

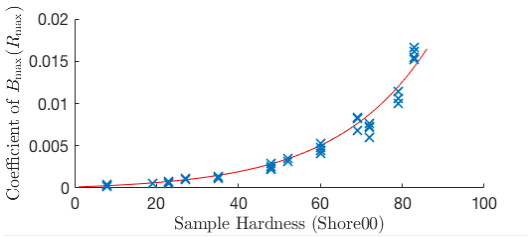

(b)

Fig. 5. (a)Maximum brightness function value $\bar{B}_{\max}$ with the contact area radius $R_{\max}$ during multiple presses. (b)The relationship of the linear coefficient of $\bar{B}_{\max}(R_{\max})$, the f_B, against $R_{\max}$ for different levels of hardness. The data is fitted with an exponential function $\hat{f}_B$.

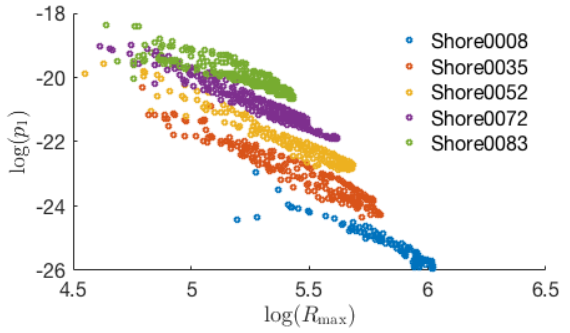

Fig. 6. Relationship of $\log(p_{1,R_{\max}})$ and $\log(R_{\max})$ for samples of different hardness levels.

the $\hat{H}$ in a single pressing sequence, where $R_{\max}$ differs.

B. Marker Motion during Press

Markers on the touch sensor surfaces help to tell the contact force by their motion (c.f., [16], [17], [18]). The GelSight sensor has specially designed black markers embedded on the elastomer surface. We track their movements during contact to infer the contact force [21]. For a thin elastomer, different kinds of force cause different movement field patterns; the resultant vector field can be approximately considered as the linear sum of the fields caused by different forces. Thus, the overall displacement field $\mathbf{\Phi}(x, y)$ has the expression

$$\mathbf{\Phi} = \mathbf{\Phi}_N + \mathbf{\Phi}_S + \mathbf{\Phi}_T, \tag{2}$$

where $\mathbf{\Phi}_N$ is the field caused by normal force, $\mathbf{\Phi}_S$ is the field caused by shear force, and $\mathbf{\Phi}_T$ is the field caused by torque. In this set of experiments of pressing GelSight on

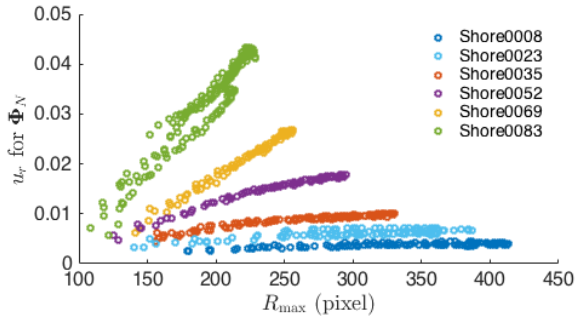

(a)

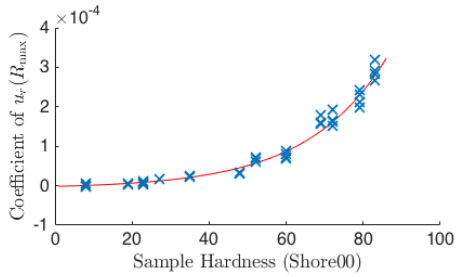

(b)

Fig. 7. (a)The relationship of u_r and the contact area radius $R_{\max}$, for samples of different hardness levels. (b)The coefficient f_M for $u_r(R_{\max})$, and its fitted curve $\hat{f}_M$.

hemispheres, the contact geometry is rotationally symmetric, and the shear force is relatively small so that no partial slip exists. We can thus write the displacement field in polar coordinates $\mathbf{e}_r, \mathbf{e}_\theta$ with the origin as the contact center, so that within the contact region, we have the following relationship:

$$\begin{aligned} \mathbf{\Phi}_N(r,\theta) &= U_r(r)\mathbf{e}_r \\ \mathbf{\Phi}_S(r,\theta) &= u_x\mathbf{e}_x + u_y\mathbf{e}_y \\ \mathbf{\Phi}_T(r,\theta) &= U_\theta(r)r\mathbf{e}_\theta \end{aligned} \tag{3}$$

According to experimental results, in this experiment we can simplify $U_r(r)$ and $U_\theta(r)$ as

$$U_r(r) = u_r r, U_\theta(r) = u_\theta \tag{4}$$

u_r, u_θ, u_x, u_y are all constants related to the magnitudes of the external force or torque. As a first approximation, we can assume they are linearly related to the force or torque magnitudes. We decompose the displacement field $\mathbf{\Phi}$ within the contact area according to (4) and (3). For hardness measurement, we only use $\mathbf{\Phi}_N$ because the normal force is dominant.

We decompose $\mathbf{\Phi}$ using a method that combines image registration and image pyramids. First, we mark the contact area for the press according to the image brightness, and consider $\mathbf{\Phi}$ as an entity as shown in (3), so that a motion is a 4DOF vector $[u_x, u_y, u_r, u_\theta]^T$. The vector is calculated using image registration, from different scales of the image.

Figure 3(c)(g) shows examples of the marker displacement field $\mathbf{\Phi}$, and the corresponding $\mathbf{\Phi}_N$ in the contact area shown in (d)(h). The two examples are pressing experiments with

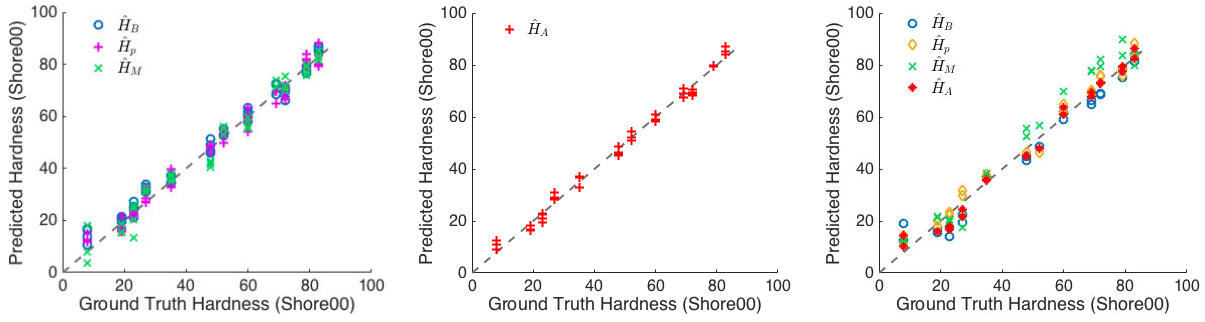

Fig. 8. Hardness prediction on R12.7mm samples. (a)$\hat{H}_B$, $\hat{H}_p$, $\hat{H}_M$ on training dataset. (b)Final prediction $\hat{H}_A$ based on a linear combination of $\hat{H}_B$, $\hat{H}_p$ and $\hat{H}_M$. (c)Prediction on a testing dataset. Data acquired by a compliant robot with no force control.

different levels of hardness, so that although the contact area is the same, the magnitudes of $\mathbf{\Phi}$ differ. Pressing on softer samples makes smaller u_rs, indicating that the normal forces are relatively smaller. In the loading period, u_r also increases as the contact radius $R_{\max}$ and the normal force increase. The relationship of u_r to $R_{\max}$ is shown in Figure 7(a), and we can see when pressing on the same sample, they are approximately of a linear relationship $u_r(R_{\max}) = f_M R_{\max} + p_0$. The linear coefficient f_M is positive with respect to sample hardness, as shown in Figure 7(b). We fit an offset exponential function $\hat{f}_M = A_M \exp(B_M \times H) + C_M$ for f_M, so that we can predict the hardness $\hat{H}_M$ from measured f_M in a pressing sequence.

C. Hardness Prediction

According to Section V-A, V-B, we can obtain three hardness prediction $\hat{H}_B$, $\hat{H}_p$ and $\hat{H}_M$ from a sequence of GelSight signal during a single press. We make a hardness prediction $\hat{H}_A$ as the linear combination of the three predictions, such that

$$\hat{H}_A = \begin{bmatrix} \hat{H}_B & \hat{H}_p & \hat{H}_M & 1 \end{bmatrix} \mathbf{b}_A \tag{5}$$

Vector $\mathbf{b}_A$ is trained through linear regression.

VI. Experimental Results

A. One-size hemispherical samples

The hardness of silicone hemispheres can be predicted using the model introduced in Section V. We start with the samples of a single size (a radius of 12.7mm), and made 12 samples with hardness ranging from Shore0008 to Shore0083, and took 46 pressing sequences of them for parameter training. On the training dataset, the prediction $\hat{H}_B$, $\hat{H}_p$, $\hat{H}_M$, which are for different features, are shown in Figure 8(a), and the fitting error shown in Table I. The overall prediction $\hat{H}_A$ is shown in Figure 8(b), and the error shown in Table I. Those results show that the separate and overall hardness predictions are all very close to the ground truth on the training dataset, with an R^2 (coefficient of determination) of 0.9978 and a root mean square error (RMSE) of 2.18 on Shore00 scale. In a 10-fold cross validation test, the RMSE ranges from 0.8441 to 3.8849, with the mean being 2.4279 and the standard deviation 0.6771.

TABLE I

Prediction error on training and testing dataset for R12.7mm hemispherical samples

	$\hat{H}_B$	$\hat{H}_p$	$\hat{H}_M$	$\hat{H}_A$
R^2 train (human data)	0.9946	0.9954	0.9921	0.9978
RMSE train (human data)	3.4123	3.1539	4.1147	2.1846
R^2 test (robot data)	0.9910	0.9951	0.9794	0.9952
RMSE test (robot data)	4.4349	3.2777	6.7078	3.2218

We collected a test dataset of 24 pressing sequences using a Baxter robot on the samples. We mounted the sensor on the robot gripper, and made the robot press on samples in a fixed open-loop routine. The robot's force and displacement are not well controlled, and there is large unknown variability in different presses, especially on the contact force. The variability of robot tester is much larger than that of human testers. The results from the test dataset using Baxter are shown in Figure 8(c), and the error in Table I. The figure and table show that the hardness prediction matches the ground truth well, with R squared of 0.9952 and RMSE of 3.22 in Shore00, although the data is taken in a totally different way with different manipulation error types. Among the predictions, $\hat{H}_p$ is the most stable, and $\hat{H}_M$ makes the largest error, most likely because the robot introduces large noise in pressing force during the measurement, leading to a u_r measurement that makes much larger error. The final result shows that our model is very stable in the unknown pressing modes.

B. Hemisphere samples of different sizes

We test the GelSight measurement on silicone hemispheres of different sizes using the same training model from Section VI-A. New samples are with radii r_s of 30mm, 19mm and 9.5mm, and hardness ranging from Shore0008 to Shore0083. Figure 9 shows brightness function B and the marker displacement field $\mathbf{\Phi}_N$ when pressing on the samples of the same H (Shore0035) but different r_s. The figures show that B and $\mathbf{\Phi}_N$ are shaped similarly for different r_s samples,

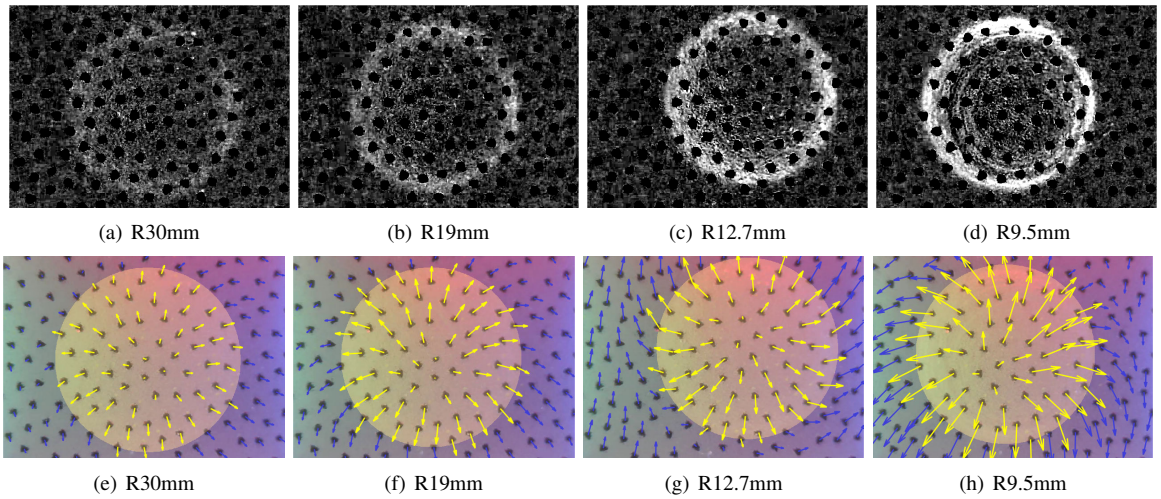

(a) R30mm (b) R19mm (c) R12.7mm (d) R9.5mm

(e) R30mm (f) R19mm (g) R12.7mm (h) R9.5mm

Fig. 9. GelSight data on Shore0035 samples of different radius r_s. Frames are taken from pressing sequences, and are specifically chosen as the moment when contact areas are the same. The first row shows brightness change function B; the second row shows marker displacement field caused by normal force ($\mathbf{\Phi}_N$). Figures show that when H and $R_{\max}$ are the same, smaller r_s results in larger B value and larger $\mathbf{\Phi}_N$.

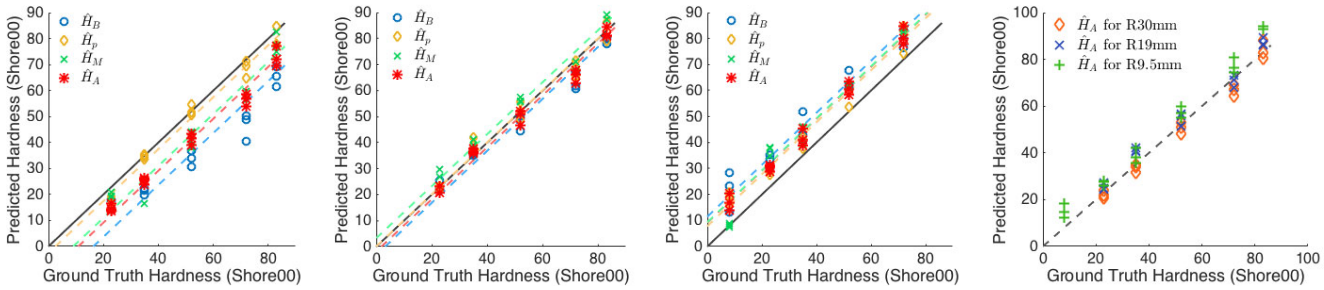

(a) (b) (c) (d)

Fig. 10. Hardness prediction for samples of different radii, using the numerical model trained on R12.7mm samples. (a)Hardness prediction for R30mm sample. (b)Hardness prediction for R19mm sample. (c)Hardness prediction for R9.5mm sample. (d)$\hat{H}_A$ when using normalized linear measurement $\hat{R}$.

TABLE II

R SQUARED FOR H PREDICTION OF DIFFERENT SAMPLE RADII

Sample	$\hat{H}_B$	$\hat{H}_p$	$\hat{H}_M$	$\hat{H}_A$
R30mm	0.7768	0.9880	0.9237	0.9084
R30mm (shifted)	0.9680	0.9926	0.9818	0.9927
R19mm	0.9819	0.9907	0.9822	0.9908
R19mm (shifted)	0.9890	0.9907	0.9898	0.9931
R9.5mm	0.9273	0.9651	0.9482	0.9555
R9.5mm (shifted)	0.9899	0.9941	0.9895	0.9952

TABLE III

RMSE FOR H PREDICTION OF DIFFERENT SAMPLE RADII

Sample	$\hat{H}_B$	$\hat{H}_p$	$\hat{H}_M$	$\hat{H}_A$
R30mm	17.6611	4.0970	10.3246	11.3127
R30mm (shifted)	6.6850	3.2177	5.0460	3.1913
R19mm	5.0352	3.6117	4.9824	3.5942
R19mm (shifted)	3.9252	3.6099	3.7666	3.1036
R9.5mm	12.3616	8.5665	10.4372	9.6737
R9.5mm (shifted)	4.6055	3.5117	4.6957	3.1872

but for smaller r_s samples, when $R_{\max}$ is the same, both B and u_r are larger.

In general, when pressing on samples of different r_s, B and u_r have a similar relationship to $R_{\max}$ as shown in Figure 5, Figure 6, and Figure 7, but the parameters differ. Using the model in Section VI-A, the hardness prediction results are shown in Figure 10(a)(b)(c), and prediction error in Table II and III. The figures show that for samples of the same r_s, the hardness predictions are not precise, but the relative hardness prediction is still correct, which is shifted to the ground truth with a constant related to the sample radius. After compensating for the shift by using an offset acquired by the average predictions, the prediction error is greatly reduced, as shown in Table II and III. It can be seen that after the shift, the predictions have very small error, with RMSE around 3.1 Shore00, and the shifted value is a constant about r_s.

In real measurement cases, the average prediction is unknown but the sample radius r_s might be known. We use a normalized radical measurement $\hat{R} = \frac{r_{s0}}{r_s} R$ for all the feature calculation, where r_{s0} is the radius of the training sample set (12.7mm). In this scenario, it is easy to calculate that the $\hat{H}_B$, $\hat{H}_p$, $\hat{H}_M$ based on $\hat{R}$ are all shifted for a constant, and the constant is only related to r_s. We make new hardness predictions using $\hat{R}$, and show the $\hat{H}_A$ prediction in

Figure 10(d). The figure shows that the hardness prediction results are close to ground truth for different r_s, the R^2 for overall prediction is is 0.9892, and RMSE is 5.06 in Shore00 scale. The good prediction results indicate that given samples of known hemispherical shape, we can measure the hardness using the normalized scale $\hat{R}$ and the numerical model trained on samples of a different radius as described in Section VI-A.

VII. Conclusion

In this paper, we show a method of estimating object hardness with a GelSight tactile sensor. We press the sensor on the object using loosely controlled movement, and the deformation of the elastomer on the sensor reflects the object hardness. We estimate the object hardness by comparing the change in the contact area and contact surface geometry as well as a measure of the normal force during the press. Geometric features can be inferred from the GelSight image intensity change, and the normal force can be estimated by the marker movement on the sensor surface. We show that for the silicone samples of the same geometry, both the image intensity and marker displacement magnitude increases as the contact area increases during pressing. No external sensing information is required for the measurement. For the hemispherical samples, we propose a numerical model to estimate sample hardness, and conduct experiments to show that the model can predict sample hardness with only a small error.

In the future, we plan to work further on generalizing the hardness estimation model for objects of arbitrary shapes. In our preliminary experiments on a variety of object shapes, we used cylinders, edges, flat embossed and random embossed objects. When contacting objects are of the same shape but with different hardness, B and u_r increase as the contact area increases, and for harder samples B and u_r are larger than for the soft ones, which could be used for hardness estimation. Two examples are shown in Figure 2. However, the corresponding relationship is closely related to the surface geometry, which will be explored in our future work.

Acknowledgment

The work is supported by a grant from Shell to EHA and ERC-2009-AdG 247041 to MAS. The authors would like to thank Erik Hemberg, Shaiyan Keshvari, Xinchen Ni, Andrea Censi, Alyanna Villapandos, Siyuan Dong for their suggestions and help in experiments.

References

[1] R. D. Howe, "Tactile sensing and control of robotic manipulation," *Advanced Robotics*, vol. 8, no. 3, pp. 245–261, 1993.

[2] A. Drimus, G. Kootstra, A. Bilberg, and D. Kragic, "Design of a flexible tactile sensor for classification of rigid and deformable objects," *Robotics and Autonomous Systems*, vol. 62, no. 1, pp. 3–15, 2014.

[3] V. Chu, I. McMahon, L. Riano, C. G. McDonald, Q. He, J. Martinez Perez-Tejada, M. Arrigo, N. Fitter, J. C. Nappo, T. Darrell, *et al.*, "Using robotic exploratory procedures to learn the meaning of haptic adjectives," in *Robotics and Automation (ICRA), 2013 IEEE International Conference on*. IEEE, 2013, pp. 3048–3055.

[4] M. A. Srinivasan and R. H. LaMotte, "Tactual discrimination of softness," *Journal of Neurophysiology*, vol. 73, no. 1, pp. 88–101, 1995.

[5] M. K. Johnson and E. Adelson, "Retrographic sensing for the measurement of surface texture and shape," in *Computer Vision and Pattern Recognition (CVPR), 2009 IEEE Conference on*. IEEE, 2009, pp. 1070–1077.

[6] M. K. Johnson and E. H. Adelson, "Shape estimation in natural illumination," in *Computer Vision and Pattern Recognition (CVPR), 2011 IEEE Conference on*. IEEE, 2011, pp. 2553–2560.

[7] S. J. Lederman and R. L. Klatzky, "Extracting object properties through haptic exploration," *Acta psychologica*, vol. 84, no. 1, pp. 29–40, 1993.

[8] W. M. B. Tiest, "Tactual perception of material properties," *Vision research*, vol. 50, no. 24, pp. 2775–2782, 2010.

[9] W. M. B. Tiest and A. M. Kappers, "Cues for haptic perception of compliance," *IEEE Transactions on Haptics*, vol. 2, no. 4, pp. 189–199, 2009.

[10] Z. Su, J. A. Fishel, T. Yamamoto, and G. E. Loeb, "Use of tactile feedback to control exploratory movements to characterize object compliance," *Active Touch Sensing*, p. 51, 2014.

[11] T. Shimizu, M. Shikida, K. Sato, and K. Itoigawa, "A new type of tactile sensor detecting contact force and hardness of an object," in *Micro Electro Mechanical Systems, 2002. The Fifteenth IEEE International Conference on*. IEEE, 2002, pp. 344–347.

[12] S. Okamoto, M. Konyo, Y. Mukaibo, T. Maeno, and S. Tadokoro, "Real-time estimation of touch feeling factors using human finger mimetic tactile sensors," in *2006 IEEE/RSJ International Conference on Intelligent Robots and Systems*. IEEE, 2006, pp. 3581–3586.

[13] S. Omata and Y. Terunuma, "New tactile sensor like the human hand and its applications," *Sensors and Actuators A: Physical*, vol. 35, no. 1, pp. 9–15, 1992.

[14] O. Lindahl, S. Omata, and K.-A. Ängquist, "A tactile sensor for detection of physical properties of human skin in vivo," *Journal of medical engineering & technology*, vol. 22, no. 4, pp. 147–153, 1998.

[15] M. Takei, H. Shiraiwa, S. Omata, N. Motooka, K. Mitamura, T. Horie, T. Ookubo, and S. Sawada, "A new tactile skin sensor for measuring skin hardness in patients with systemic sclerosis and autoimmune raynaud's phenomenon," *Journal of international medical research*, vol. 32, no. 2, pp. 222–231, 2004.

[16] N. J. Ferrier and R. W. Brockett, "Reconstructing the shape of a deformable membrane from image data," *The International Journal of Robotics Research*, vol. 19, no. 9, pp. 795–816, 2000.

[17] K. Kamiyama, K. Vlack, T. Mizota, H. Kajimoto, K. Kawakami, and S. Tachi, "Vision-based sensor for real-time measuring of surface traction fields," *IEEE Computer Graphics and Applications*, vol. 25, no. 1, pp. 68–75, 2005.

[18] C. Chorley, C. Melhuish, T. Pipe, and J. Rossiter, "Development of a tactile sensor based on biologically inspired edge encoding," in *Advanced Robotics, 2009. ICAR 2009. International Conference on*. IEEE, 2009, pp. 1–6.

[19] X. Jia, R. Li, M. A. Srinivasan, and E. H. Adelson, "Lump detection with a gelsight sensor," in *World Haptics Conference (WHC), 2013*. IEEE, 2013, pp. 175–179.

[20] R. Li, R. Platt, W. Yuan, A. ten Pas, N. Roscup, M. A. Srinivasan, and E. Adelson, "Localization and manipulation of small parts using gelsight tactile sensing," in *Intelligent Robots and Systems (IROS 2014), 2014 IEEE/RSJ International Conference on*. IEEE, 2014, pp. 3988–3993.

[21] W. Yuan, R. Li, M. A. Srinivasan, and E. H. Adelson, "Measurement of shear and slip with a gelsight tactile sensor," in *Robotics and Automation (ICRA), 2015 IEEE International Conference on*. IEEE, 2015, pp. 304–311.